IJHSR ijhighschoolresearch.org
RESEARCH ARTICLE

Computational Analysis of Non-Linear Models in Predicting the Anisotropic Reynolds Stress Tensor for Turbulent Flow

Aiden J. Kwon

Palos Verdes Peninsula High School, 27118 Silver Spur Road, Rolling Hills Estates, CA, 90274, USA; aidenkwon3@gmail.com

ABSTRACT: Direct Numerical Simulation (DNS) is the most accurate method for simulating turbulent flow, but its high computational cost makes it impractical for standard industrial use. The Reynolds Averaged Navier-Stokes (RANS) approach is widely used as an alternative. However, RANS relies on Reynolds stress modeling to address the closure problem, which presents challenges. Most RANS models use Linear Eddy Viscosity Models (LEVM), which struggle to accurately predict complex flows, such as those with severe flow separation, high swirling flow, and high surface curvature. This research conducts a computational study of Non-Linear Eddy Viscosity Models (NLEVM) to improve anisotropic Reynolds stress tensor predictions. Various NLEVMs are investigated, including the Pope algebraic stress model, the Gatski algebraic stress model, the Spalart second-order closure model, and the Speziale-Gatski (SSG) second-order closure model. Numerical Reynolds stress tensor components computed using the NLEVM approach are analyzed using DNS datasets for a two-dimensional converging-diverging channel and a three-dimensional square duct. The research found that NLEVMs are inconsistent in achieving higher accuracy for all Reynolds stress components compared to LEVMs. Improving accuracy using empirical coefficients of scalar functions for higher-order tensor bases in the non-linear expansion remains challenging.

KEYWORDS: Physics and Astronomy Mechanics, Turbulence, Computational Fluid Dynamics, Reynolds Stress Tensor.

Introduction

Over 500 years ago, Leonardo da Vinci identified turbulence as a unique fluid behavior. He coined the term "turbolenze" to describe these fluid motions, which become "turbulence" in the modern day. However, it was not until the early 20th century that scientists developed a rigorous mathematical framework to understand turbulence. In contrast to laminar flow, turbulent flow is mostly observed in nature. Given the widespread impact of turbulence on engineering and scientific advancements, it is essential to have a solid physical understanding of turbulent flow. Today, there are many numerical approaches available to simulate turbulent flows. The most popular mathematical frameworks among all are Direct Numerical Simulation (DNS), Large Eddy Simulation (LES), and Reynolds Averaged Navier-Stokes (RANS). DNS is considered the most accurate computational approach. However, its high computational cost has remained an impractical application for standard industrial use. LES can resolve large-scale turbulence while effectively modeling small-scale eddies. This makes LES a more affordable option than DNS, but it remains inefficient for high Reynolds number flow, which dominates most industrial cases. Among these models, RANS is the most cost-effective alternative as the new RANS formulation eliminates temporal terms of the original Navier-Stokes equation. This allows the solution to be computed in steady-state form. This steady-state approach requires far fewer computational resources than DNS and LES and is popular in the industry. However, the RANS approach introduced a new term called the Reynolds stress tensor that requires turbulence modeling closure. Figure 1 shows the hierarchy of these popular computational methods highlighting trade-offs based on computational cost and prediction accuracy.

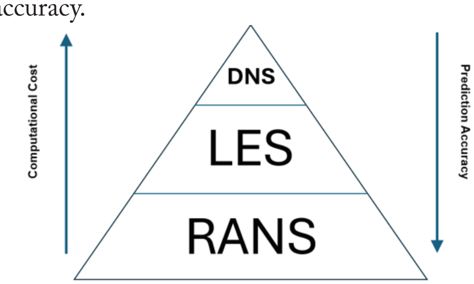

Figure 1: Comparison of popular computational methodologies and their relative computational cost and prediction accuracy. RANS provides the most cost-effective approach but is compromised by prediction accuracy.

The momentum equation of RANS is given by the following:

$$\frac{\partial u_i}{\partial t} + u_j \frac{\partial u_i}{\partial x_j} = -\frac{1}{\rho}\frac{\partial p}{\partial x_i} + \frac{\partial}{\partial x_j}\left(\frac{\mu}{\rho}\frac{\partial u_i}{\partial x_j}\right) \tag{1}$$

Reynolds-averaged quantities are defined as the following:

$$\begin{aligned} u_i(x_k,t) &= U_i(x_k) + u'(x_k,t) \\ U_i(x_k) &= \lim_{T\to\infty}\frac{1}{T}\int_0^T u(x_k,t)dt \end{aligned} \tag{2}$$

Substitute and average:

$$U_j\frac{\partial U_i}{\partial x_j} = -\frac{1}{\rho}\frac{\partial P}{\partial x_i} + \frac{\partial}{\partial x_j}\left(\frac{\mu}{\rho}\frac{\partial U_i}{\partial x_j}\right) + \frac{\partial\left(-\overline{u_i'u_j'}\right)}{\partial x_j} \tag{3}$$

where u_i is the instantaneous fluid velocity, U_i is the mean fluid velocity, and u_i' is a component of velocity fluctuation.

Compared to Equation 1, Equation 3 has eliminated temporal terms by adding the Reynolds stress tensor term. This Reynolds stress tensor is not a fluid property but a flow property. Due to the need to compute the Reynolds stress tensor,

  DOI: 10.36838/v7i2.1

different variations of RANS-based formulations have arisen, including zero-equation, one-equation, and two-equation models. Zero-equation solves partial differential equations (PDE) related to the mean velocity field. A one-equation model solves PDE related to the turbulence velocity field. The two-equation model solves PDEs associated with the turbulent velocity and length scale. Furthermore, these eddy viscosity models adopt Linear Eddy Viscosity Models (LEVM) or Non-Linear Eddy Viscosity Models (NLEVM).

Linear Eddy Viscosity Models (LEVM):

LEVM is easy to implement and is based on Boussinesq's hypothesis with the following linear constitutive equation:

$$\rho\overline{u_i'u_j'} = \mathrm{a}_{ij} + \frac{2}{3}k\delta_{ij} \qquad (4)$$

where

$$\mathrm{a}_{ij} = -2v_t S_{ij}$$

$$S_{ij} = \frac{1}{2}\left(\frac{\partial U_i}{\partial x_j} + \frac{\partial U_j}{\partial x_i}\right)$$

$$k = \frac{1}{2}\overline{u_i u_i}$$

a_{ij} is the Reynolds stress tensor, v_t is a scalar coefficient called turbulent viscosity (sometimes called 'effective viscosity'), and S_{ij} is the mean strain rate tensor. k is the turbulent kinetic energy, and δ_{ij} is the Kronecker delta.

The Boussinesq equation describes the linear relation between stress and strain tensors. Although a common application, LEVMs are unable to predict complex, anisotropic flow.[1] Specifically, secondary flow in different geometries are difficult for LEVMs to predict. A non-linear form of the stress tensor was created to make up for the shortcomings of LEVMs.

Non-linear Eddy Viscosity Models (NLEVM):

NLEVM is called the algebraic Reynolds stress model, which uses algebraic formulations to represent non-linear terms. Unlike isotropic LEVM, NLEVM aims to give a more realistic representation of turbulent properties by defining turbulent properties dependent on direction as anisotropic. For example, anisotropic turbulent velocities at different directions can be characterized by the following non-equivalent relation:

$$\overline{u'u'} \neq \overline{v'v'} \neq \overline{w'w'} \qquad (5)$$

where $\overline{u'u'}$ is the turbulent fluctuating velocity component in the x-direction in a cartesian coordinate system, $\overline{v'v'}$ is in the y-direction, and $\overline{w'w'}$ is in the z-direction.

Lumley first proposed NLEVM.[2] NLEVM typically utilizes quadratic and cubic equations. Most NLEVM relies on high-order products for the mean strain and rotation rate tensors. This often results in inconsistent improvement over LEVM, so adoption in the industry has been slow.

In 1973, Pope set the foundation for NLEVM by formulating a non-linear analytical equation to solve for the anisotropic Reynolds stress tensor.[3] Pope has derived the algebraic expansion of a general form of anisotropic tensors based on its relevant integrity basis. It is shown that the anisotropic tensor of a general eddy viscosity model for incompressible flow can be expressed as a combination of 10 tensor bases and 5 invariants. Consistent with physical constraints, these tensor bases naturally satisfy Galilean invariance. Caley-Hamilton's theory further allows the expression of the anisotropic tensor to be defined with a set of a finite number of tensor bases, which is practical for numerical computation. In 1992, Gatski's research showed further application by developing algebraic stress models for turbulence.[4] These stress models would circumvent the need for differential equations, which allows for more computationally efficient predictions for higher-order terms. In addition, the Speziale-Gatski (SSG) model is also introduced as a second-order closure approach based on the regularized algebraic stress model.[4] Given that the SSG model is easier to implement without higher order terms, it provides an advantage for real-world applications as the computational cost is often a major restriction. In 2000, Spalart demonstrated the Spalart-Allmaras (S-A) model for the first time, which is used in conjunction with the non-Boussinesq constitutive equation to improve eddy-viscosity approximation. Their square duct test result is quite promising, where the secondary flow in the corners matches the experimental data well. However, 3D wall jets have not been successful with this model. This could be due to the second-order closure limitations of the model.[5]

Recently, Modesti carried out an a priori test of LEVM and NLEVM using DNS data of 3D square duct flow up to friction Reynolds number of, Re = 1,055.[6] The research provides evidence that NLEVM, using higher order polynomial expansions, is more accurate compared to LEVM. Consistent with past research, LEVM suffers limited accuracy when predicting complex flows with significant anisotropies. Motivated by Modesti's approach of interrogating each scalar function term of Pope's algebraic Reynolds stress model, this research expands further the numerical investigation using Gatski's algebraic Reynolds stress model, Spalart's second-order closure model, and SSG's second-order closure model.

This research aims to evaluate the numerically anisotropic Reynolds stress tensor for high Reynolds number turbulent flow with both LEVM and NLEVM approximations. Both a two-dimensional converging-diverging channel and a three-dimensional square duct are investigated. The qualitative and quantitative numerical results of dominating Reynolds stress tensor components are presented, comparing both LEVM and NLEVM approaches. The Boussinesq hypothesis is used for LEVM. For NLEVM, four variations are implemented and investigated, including Pope's algebraic stress model, Gatski's algebraic stress model, Spalart's second-order closure model, and SSG's second-order closure model, respectively.

Methods

This research study uses numerical methods to compute the Reynolds stress tensor. The numerically predicted Reynolds stress tensor of LEVM and NLEVM closure models are computed based on DNS mean flow data. All closure models are numerically validated against DNS turbulence data. The validation provides insight into the accuracy of the closure models before applying them to RANS. Since the Boussinesq-based LEVM formulation was given in Equation 4 in the previous section, only NLEVM formulations are presented and explained in this section. Four different NLEVM variations are investigated, namely: (1) Pope algebraic stress model, (2) Gatski algebraic stress model, (3) Spalart second-order closure model, and (4) SSG second-order closure model. Despite Pope's model being the general formulation for both LEVM and NLEVM, higher-order terms are difficult to implement computationally. In contrast, the Gatski model attains higher-order terms more easily. Despite the Spalart and SSG models being second order, the formulations are relatively easy to implement.

Pope Algebraic Stress Model:

The exact presentation of the anisotropic tensor using the Pope algebraic Reynolds stress model is described as the following:

$$a_{ij} = \sum_{n=1}^{N} G^{(n)}\mathrm{T}^{(n)} \qquad (6)$$

where $\quad N = 1, \ldots, 10$

where the coefficients $G^{(n)}$ are scalar functions of invariants and $\mathrm{T}^{(n)}$ is a set of ten independent tensor bases defined by the following:

$$\begin{aligned}
&\mathrm{T}^{(1)} = \mathrm{S} && \mathrm{T}^{(2)} = \mathrm{S}\Omega - \Omega\mathrm{S} \\
&\mathrm{T}^{(3)} = \mathrm{S}^2 - \tfrac{1}{3}\mathrm{I}\{\mathrm{S}^2\} && \mathrm{T}^{(4)} = \Omega^2 - \tfrac{1}{3}\mathrm{I}\{\Omega^2\} \\
&\mathrm{T}^{(5)} = \Omega\mathrm{S}^2 - \mathrm{S}^2\Omega && \mathrm{T}^{(6)} = \Omega^2\mathrm{S} + \mathrm{S}\Omega^2 - \tfrac{2}{3}\mathrm{I}\{\mathrm{S}\Omega^2\} \\
&\mathrm{T}^{(7)} = \Omega\mathrm{S}\Omega^2 - \Omega^2\mathrm{S}\Omega && \mathrm{T}^{(8)} = \mathrm{S}\Omega\mathrm{S}^2 - \mathrm{S}^2\Omega\mathrm{S} \\
&\mathrm{T}^{(9)} = \Omega^2\mathrm{S}^2 + \mathrm{S}^2\Omega^2 - \tfrac{2}{3}\mathrm{I}\{\mathrm{S}^2\Omega^2\} && \mathrm{T}^{(10)} = \Omega\mathrm{S}^2\Omega^2 - \Omega^2\mathrm{S}^2\Omega
\end{aligned} \qquad (7)$$

where S is the mean strain rate tensor and Ω is the mean rotation rate tensor. S is a symmetrical tensor, while Ω is a skewed symmetrical tensor. In the analysis section of this paper, ~ is used as the overhead of the Reynolds stress tensor to represent the tensor's components that closure models strictly model. Both tensors are defined as the following:

$$S_{ij} = \frac{1}{2}\left(\frac{\partial U_i}{\partial x_j} + \frac{\partial U_j}{\partial x_i}\right) \qquad (8)$$

$$\Omega_{ij} = \frac{1}{2}\left(\frac{\partial U_i}{\partial x_j} - \frac{\partial U_j}{\partial x_i}\right) \qquad (9)$$

The five invariants are defined below based on the variations of both tensors and taking the trace operation { }:

$$\{\mathrm{s}^2\},\ \{\Omega^2\},\ \{\mathrm{s}^3\},\ \{\Omega^2\mathrm{s}\},\ \{\Omega^2\mathrm{s}^2\}$$

From Equation 6, when N=1, the anisotropic tensor representation is reduced to a linear form equal to the Boussinesq linear isotropic tensor. By setting N=1 and using the first tensor basis, $\mathrm{T}^{(1)}$=S, it can be determined that {aS}= $G^{(1)}$\{SS\}. Recognizing that $G^{(1)} = -2v_t$, we get the following:

$$v_t = -\frac{G^{(1)}}{2} = -\frac{\{\mathrm{aS}\}}{2\{\mathrm{SS}\}} \qquad (10)$$

From Equation. 6, when N=2, the scalar function $G^{(2)}$ can be obtained as the following:

$$G^{(2)} = \frac{\{(a + 2v_t\mathrm{S})(\mathrm{S}\Omega - \Omega\mathrm{S})\}}{\{(\mathrm{S}\Omega - \Omega\mathrm{S})(\mathrm{S}\Omega - \Omega\mathrm{S})\}}$$

Once $G^{(1)}$ and $G^{(2)}$ are computed, Equation 6 is used to compute the anisotropic tensor components. To obtain further higher-order terms of G with an analytical approach, the Gatski algebraic stress model below is used as it is much more efficient and easier to implement.

Gatski Algebraic Stress Model:

Based on the foundation set by Pope's formulation, Gatski extended the analysis of Pope to allow easier implementation for higher-order terms. These higher-order terms of the scalar functions of Equation 6 can be expressed explicitly as the following:

$$\begin{aligned}
&G^{(1)} = -\tfrac{1}{2}(6 - 3\eta_1 - 21\eta_2 - 2\eta_3 + 30\eta_4)/D && G^{(6)} = -9/D \\
&G^{(2)} = -(3 + 3\eta_1 - 6\eta_2 + 2\eta_3 + 6\eta_4)/D && G^{(7)} = 9/D \\
&G^{(3)} = (6 - 3\eta_1 - 12\eta_2 - 2\eta_3 - 6\eta_4)/D && G^{(8)} = 9/D \\
&G^{(4)} = -3(3\eta_1 + 2\eta_3 + 6\eta_4)/D && G^{(9)} = 18/D \\
&G^{(5)} = -9/D && G^{(10)} = 0
\end{aligned} \qquad (11)$$

$$D = 3 - \frac{7}{2}\eta_1 + \eta_1^2 - \frac{15}{2}\eta_2 - 8\eta_1\eta_2 + 3\eta_2^2 - \eta_3 + \frac{2}{3}\eta_1\eta_3 - 2\eta_2\eta_3 + 21\eta_4 + 24\eta_5 + 2\eta_1\eta_4 - 6\eta_2\eta_4$$

$$\eta_1 = \{S^{*2}\}$$
$$\eta_2 = \{\Omega^{*2}\}$$
$$\eta_3 = \{S^{*3}\}$$
$$\eta_4 = \{S^{*}\Omega^{*2}\}$$
$$\eta_5 = \{S^{*2}\Omega^{*2}\}$$

Unlike Pope's formulation, Gatski introduced non-dimensional variables for the mean strain rate tensor, mean rotation rate tensor, and anisotropic tensor. These non-dimensional tensors are related to their dimensional counterpart as the following:

$$\begin{aligned}
S^*_{ij} &= \tfrac{1}{2}g\tau(2 - C_3)S_{ij} \\
\Omega^*_{ij} &= \tfrac{1}{2}g\tau(2 - C_4)\Omega_{ij} \\
b^*_{ij} &= \left(\frac{C_3 - 2}{C_2 - \frac{4}{3}}\right)b_{ij}
\end{aligned} \qquad (12)$$

$$b_{ij} = \frac{1}{2}g\tau\left[\left(C_2 - \frac{4}{3}\right)S_{ij} + (C_3 - 2)\left(b_{ik}S_{jk} + b_{jk}S_{ik} - \frac{2}{3}b_{mn}S_{mn}\delta_{ij}\right) + (C_4 - 2)\left(b_{ik}\Omega_{jk} + b_{jk}\Omega_{ik}\right)\right]$$

$$g = \left(\frac{1}{2}C_1 + \frac{\mathcal{P}}{\epsilon} - 1\right)^{-1}$$

$$\tau = \frac{k}{\epsilon}$$

where ε is turbulent dissipation rate, $\mathcal{P}$ is turbulent production rate. The coefficients C_1–C_4 are empirical coefficients. It can also be a function of the invariant of b_{ij} or can depend on $\mathcal{P}/\varepsilon$. Below are a few combinations reported by past research.

Launder, Reece, and Rodi model

$$C_1 = 3.0,\ C_2 = 0.8,\ C_3 = 1.75,\ C_4 = 1.31$$

Gibson and Launder model

$$C_1 = 3.6,\ C_2 = 0.8,\ C_3 = 1.2,\ C_4 = 1.2$$

Speziale, Sarkar, and Gatski model

$$C_1 = 3.4 + 1.8\mathcal{P}/\varepsilon,\ C_2 = 0.8 - 1.3\Pi_b^{1/2},\ C_3 = 1.25,\ C_4 = 0.40$$

where $\Pi_b = b_{ij}b_{ij}$

SSG second-order closure model:

The Speziale-Gatski (SSG) second-order closure model was originally developed to improve the efficacy of the regularized algebraic stress model for turbulent flow involving shear and

DOI: 10.36838/v7i2.1

rotation. The non-linear Reynolds stress tensor is written in the following form:

$$\tau_{ij} = \frac{2}{3}K\delta_{ij} - \frac{6(1+\eta^2)\alpha_1 K}{3+\eta^2+6\zeta^2\eta^2+6\zeta^2}\left[S^*_{ij} + \left(S^*_{ik}\Omega^*_{kj} + S^*_{jk}\Omega^*_{ki}\right) - 2\left(S^*_{ik}S^*_{kj} - \frac{1}{3}S^*_{kl}S^*_{kl}\delta_{ij}\right)\right] \quad (13)$$

$\alpha_1 = (C_2 - \frac{4}{3})/(C_3 - 2)$ and S^*, Ω^* are defined by Equation 12. η, and ζ can be defined by the following:

$$\eta = (S^*_{ij}S^*_{ij})^{\frac{1}{2}}, \qquad \zeta = (\Omega^*_{ij}\Omega^*_{ij})^{\frac{1}{2}}$$

Spalart second-order closure model:

The Spalart second-order closure model is based on the S-A model. The non-linear Reynolds stress tensor is defined by the following:

$$\tau_{ij} = \bar{\tau}_{ij} - c_{nl1}\left[O_{ik}\bar{\tau}_{jk} + O_{jk}\bar{\tau}_{ik}\right] \quad (14)$$

where

$$O_{ik} \equiv \frac{\partial_k U_i - \partial_i U_k}{\sqrt{\partial_n U_m \, \partial_n U_m}}$$

where $\bar{\tau}_{ij}$ is the linear Reynolds stress tensor defined by Boussinesq's Equation 4, O_{ik} is the normalized rotation tensor. c_{nl1}=3 is the constant derived from simple boundary layer theory.

In this research, progressive, incremental computations of each higher-order non-linear term are analyzed and interrogated systematically. Pope's model is used to model the Reynolds stress tensor at N=1 and N=2. Gatski's model is used for considering higher-order terms, including N=3 and N=5. Adding term from N=3 to N=5 incurs almost no extra computational cost, making N=4 redundant. In addition, Pope's expansion formulation becomes more complete when more terms are included.

Model Validation Test Cases:

All closure models in this research are validated with two test cases. A two-dimensional converging-diverging (CD) channel and a three-dimensional square duct are chosen as they are commonly used to validate turbulence models. The original high-fidelity DNS dataset for both test cases is obtained from an open-source repository. The 2D converging-diverging dataset is obtained directly from NASA's DNS dataset, an open-sourced dataset on NASA's turbulence modeling resource page.[7] The 3D square duct case is obtained from a DNS data set created at the Delft University of Technology.[8]

Both test cases' flow statistics show a high Reynolds number incompressible flow. The flow frictional Reynolds number of the 2D CD channel is Re_τ = 600, which corresponds to Re = 12,600, where Re_τ and Re are defined by the following respectively:

$$Re_\tau = \frac{u_\tau h}{\nu} \quad (15)$$

$$Re = \frac{uL}{\nu} \quad (16)$$

where $u_\tau=\sqrt{\tau_w/\rho_w}$ is fluid frictional velocity with τ_w and ρ_w being the wall shear stress and density at the wall respectively, h is the height of the duct, and u is the mean flow velocity. $\tau_w=\mu \cdot d_u/d_y$ where μ is the dynamic viscosity of the fluid. u_τ is also used to express the non-dimensional form of the Reynolds stress tensor for the analysis of this research. The channel geometry is described in Figure 2.

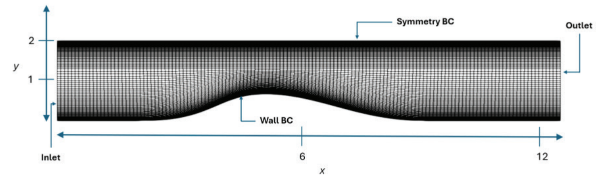

Figure 2: Geometry of 2D CD channel test case. The channel consists of inlet, outlet, wall, and symmetric boundary conditions as labeled. The fluid flow enters the channel from the left of the duct and exits towards the right. The computational domain is discretized with a total of 385 grid points in the y-direction and 2,304 grid points in the x-direction.

For the 3D square duct test case, the data set is simulated with the flow frictional Reynolds number, Re_τ = 150, which corresponds to Re = 4,410. Figure 3 shows the geometry used for this study.

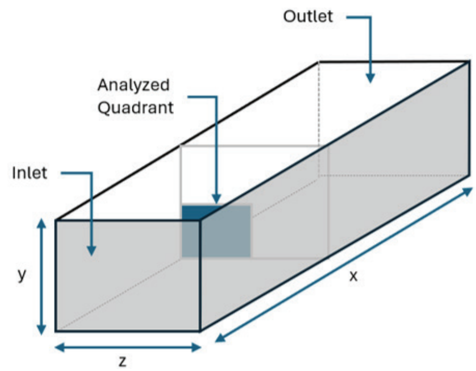

Figure 3: Geometry of 3D square duct test case. Fluid flow enters the duct from the inlet and exits through the outlet as labeled. The computational domain is discretized with a total of 128 grid points in the y-direction and 128 grid points in the z-direction. The numerical analysis for Reynolds stress model validation is performed on the lower quadrant of the fluid plane as shown.

Model Computation Process:

Jupyter Notebook computing platform implements all closure model computations and analyzes the predicted anisotropic Reynolds stress tensor. All code is written in Python. The visualization results are created using Matplotlib.[9] Figure 4 explains the model validation process. The process begins with processing DNS mean flow data. Such data is necessary to compute mean strain rate and rotation tensors using Equations 8 and 9. Once these tensors are computed, they are implemented to compute invariants necessary for Pope and Gatksi's algebraic stress models. Although both SSG and Spalart models do not utilize invariant tensors as indicated by Equations 13 and 14, both formulations require similar inputs like mean strain rate and rotation tensors. Once each model's Reynolds stress tensor is computed, their components are validated against DNS-computed Reynolds stress tensor data from the same dataset. Both test cases have different dominating Reynolds stress tensor components. For the 2D CD channel, a_{11} and a_{12} are identified as the dominating components due to being two-dimensional and symmetrical. For the 3D square duct test case, a_{11}, a_{12}, and a_{23} are the dominating components due to their influence on secondary flows in the duct and the nature of turbulence near the wall.

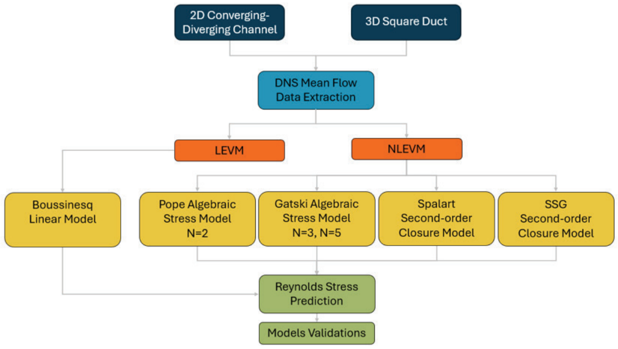

Figure 4: The complete closure model validation process is shown. The process begins with mean flow data extraction of a high-fidelity DNS dataset from two test cases. The modeling procedure includes implementing mean flow data to both LEVM and NLEVM. For this research, the linear Boussinesq-based model and a total of four different NLEVM variation models are used. NLEVM includes the Pope algebraic stress model at N=2, Gatski's algebraic stress model at N=3 and N=5, Spalart and SSG second-order models. Reynolds stress tensor components analysis is performed on all closure models developed in this research.

Result and Discussion

The following presents the numerical results of the computational analysis of two test cases with different closure models. The results show that NLEVM is inconsistently improving over LEVM. Current findings also show that the accuracy of the predicted anisotropic Reynolds stress tensor does not improve by increasing higher-order terms for NLEVM. The following analysis provides detailed insight into how NLEVM performs in these two test cases. Modelled Reynolds stress tensors are presented in non-dimensional forms by using the square of frictional fluid velocity, $u_\tau{}^2$.

2D Converging-Diverging Channel:

The following shows the results of the 2D converging-diverging channel analysis. High-fidelity DNS data from NASA is presented in Figure 5, showing the mean flow velocity component distributions. The maximum x-component velocity is found at the converging section near the peak of the wall. Overall, the y-component velocities are much weaker than the x-components as flow is predominantly in the x-direction. DNS results also show that along the positive converging wall, y-component velocity is higher tu_τ^2n the rest of the fluid domain. In contrast, along the rear diverging wall, y-component velocity turns negative due to flow separation. Flow separation near the converging area demands closure models to accurately capture anisotropic turbulence in this region.

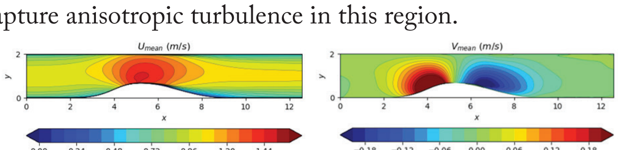

Figure 5: The contours above show DNS computed mean flow-field results for the 2D converging-diverging channel at Re_τ=600. The contours show both mean velocities in the x direction (U) and in the y direction (V), respectively. The flow separation region is indicated in blue in the y-component velocity contour. Flow separation near the converging area demands closure models to accurately capture anisotropic turbulence in this region.

Figures 6 presents comparisons of DNS computed Reynolds stress tensors to the modeling results using the LEVM-based Boussinesq model and different NLEVM variations. The detailed description of each model is also discussed below. First, the LEVM computed results are discussed, followed by SSG and Gatski's algebraic stress models.

As shown in Figure 6 (a), DNS highlights a_{11}^{+} has higher normal stress values along the near-wall region and symmetrical plane while maintaining smaller values near the center of the channel. Unlike a_{11}^{+}, a_{12}^{+} is distributed in uniform layers with higher shear stress values towards the symmetrical plane and lower values towards the wall region. The details descriptions of the remaining plots are provided in the subsequent sub-sections.

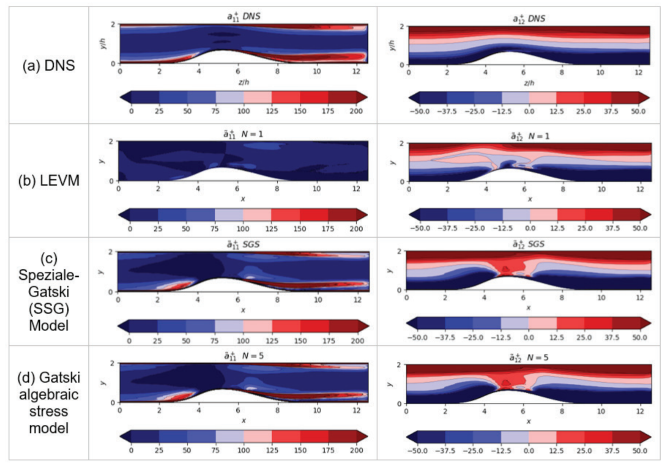

Figure 6: The comparisons of DNS computed Reynolds stress tensors to different closure modeling approaches for the 2D converging-diverging channel at Re_τ=600. Superscript + represents a non-dimensional stress tensor. Overhead symbol ~ represents the modeled Reynolds stress tensor while superscript + represents the non-dimensional stress tensor. (a) The high-fidelity DNS computed anisotropic Reynolds stress tensors, a_{11}^{+} and a_{12}^{+} show different distributions, highlighting the anisotropic behaviors of the turbulence flow. (b) The LEVM-modelled results using first order (N=1) form of Pope algebraic stress model. The modeled LEVM results are inconsistent with DNS results. (c) The Speziale-Gatski (SSG) model results show that while $\hat{a}_{11}^{+}$ closely resembles DNS data, $\hat{a}_{12}^{+}$ demonstrates inconsistencies near the converging section in the flow separation region. Even though SSG is easy to implement, it is unsuitable for complex flow modeling. (d) The Gatski algebraic stress model shows that while $\hat{a}_{11}^{+}$ is in close agreement with DNS, the modeled $\hat{a}_{12}^{+}$ results are inconsistent with DNS data.

LEVM - Boussinesq model:

As mentioned earlier, by applying N=1 to Pope algebraic stress model, Pope's formulation is reduced to and becomes the linear Boussinesq form. Unlike the DNS indication, Figure 6(b) shows the modeled $\hat{a}_{11}^{+}$ to be near uniform and retain normal stress values relatively low everywhere, including in the wall region. In addition, LEVM predicted $\hat{a}_{12}^{+}$ is found to be highly unorganized and non-uniformly distributed near the converging section. These numerical discrepancies are inconsistent with DNS. Therefore, LEVM is unsuitable for predicting the turbulent flow's anisotropic behavior. The numerical discrepancy is primarily attributed to the over-simplified linear relationship-based assumption between the Reynolds stress and mean strain rate tensor. This insight proves that LEVM-modeled normal and shear stress are not

DOI: 10.36838/v7i2.1

applicable throughout the fluid domain, especially inside the flow separation region. Turbulence is considered anisotropic, with highly non-linear flow structures in this flow separation region.

NLEVM - Speziale-Gatski (SSG) Model:

Figure 6(c) presents both models $\hat{a}_{11}^{+}$ and $\hat{a}_{12}^{+}$ using SSG second-order model. The results show that while $\hat{a}_{11}^{+}$ closely resembles DNS data, $\hat{a}_{12}^{+}$ demonstrates inconsistencies near the converging section in the flow separation region. Even though SSG is easy to implement, it is unsuitable for complex flow modeling.

NLEVM - Gatski algebraic stress model:

Figure 6(d) presents the model $\hat{a}_{11}^{+}$ and $\hat{a}_{12}^{+}$ using the Gatski model, which involves all of the first 5 terms, N=5 from Equation 11. The modeled $\hat{a}_{11}^{+}$ shows higher normal stress values at the near-wall region and symmetry plane than DNS results. However, compared to LEVM, the modeled $\hat{a}_{11}^{+}$ distribution is in better agreement with DNS in these regions. Similar to linear Boussinesq and non-linear SSG models, the modeled $\hat{a}_{12}^{+}$ also shows similar inconsistencies for shear stress values in the converging section.

Figure 7 below shows the qualitative correlation analysis between modeled anisotropic stress tensor components and their DNS counterparts. The direct comparison to DNS provides further insight into the quality and performance of the modeling accuracies. Compared to DNS, the linear Boussinesq-based model (N=1) shows strong correlations for $\hat{a}_{12}^{+}$ but weak correlations for $\hat{a}_{11}^{+}$. Overall, the analysis shows NLEVM shows slight improvement on $\hat{a}_{11}^{+}$ but no improvement on $\hat{a}_{12}^{+}$ compared to LEVM.

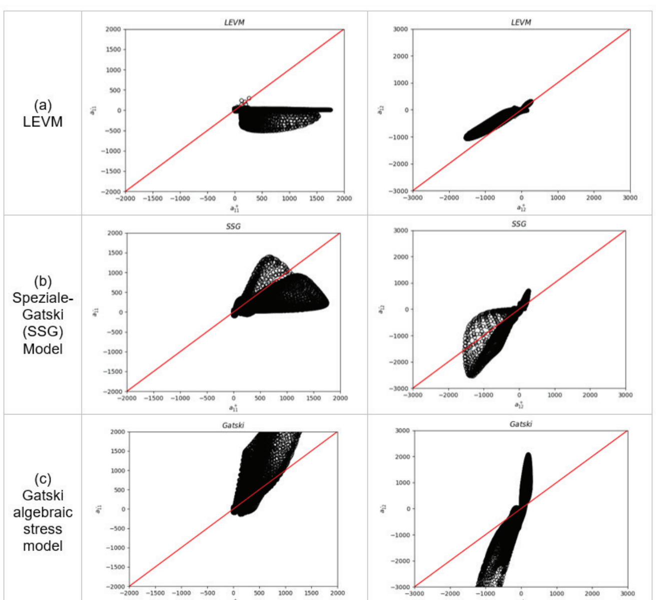

Figure 7: The qualitative analysis shows the correlation of different modelled anisotropic Reynolds stress tensors, $\hat{a}_{11}^{+}$, $\hat{a}_{12}^{+}$ and DNS computed data set for 2D converging-diverging channel at Re_{τ}=600.

In addition, both numerical errors and root mean square error analysis with respect to DNS are made available for each modeling approach in Figures 8 and 9. Although these visual plots are useful for comparative analysis similar to correlation plots, they do not adequately provide full evidence of the sources of error. Further rigorous zonal analysis can be performed to identify error sources.

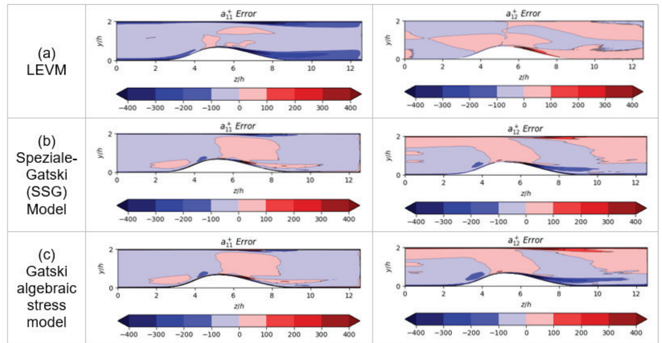

Figure 8: Comparison of numerical errors of Reynolds stress tensor components for different turbulence modeling approaches and DNS.

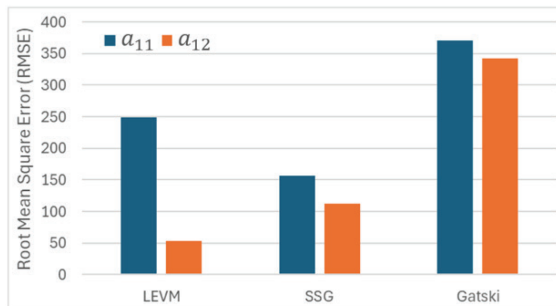

Figure 9: Comparison of numerical RMSE of Reynolds stress tensor components for different turbulence modeling approaches and DNS.

Overall, the research evidence that LEVM, the Gatski algebraic model, and the SSG model are insufficient in capturing the anisotropic shear stress components near the converging section where flow separation occurs. Next, a 3D square duct channel analysis is presented below for further interrogation of the Reynolds stress tensor components using these closure models.

3D Square Duct Channel:

The computational analysis of a 3D square duct channel is broken down into two parts. First, the results of the modeled Reynolds stress tensor distributions $\hat{a}_{12}^{+}$, $\hat{a}_{22}^{+}$, $\hat{a}_{23}^{+}$ in the lower quadrant of the channel, as indicated in Figure 3, are presented. This includes the Pope algebraic stress model at N=1 and N=2, the Gatski model at N=4 and N=5, and Spalart's second-order model. The analysis of coefficients of the scalar functions of the invariants from Pope's non-linear polynomial expansion, G are also presented. Last, a DNS comparison is presented, highlighting the correlation to all the modeling results.

Figure 8 shows the contours of the mean-flow velocity components and the secondary motions highlighted by the cross-stream V component. The high mean-flow velocity component, U in the x-direction, is shown to be distributed towards the center of the duct and is gradually reduced as it approaches the near-wall region. The velocity is zero at the wall where a non-slip boundary condition is applied. The mean-flow component in the y-direction can have distinct contours in the corners of the duct, displaying the secondary flow that occurs in the four corners. In the velocity vector field, secondary flow is also clearly visible in the corners of the duct as the vectors begin to spiral and show swirling motions. These DNS results allow us to evaluate secondary motion, specifically in the near-wall region.

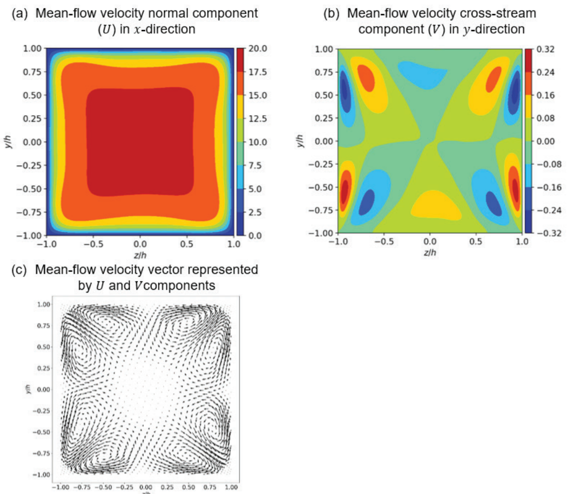

Figure 10: The contour (a) shows the mean-flow velocity component in the x-direction, (b) shows the mean-flow velocity in the y-direction, and (c) shows the vector field of both components.

Figure 9 shows the mean velocity and turbulent stress components' profiles in the lower quadrant of the square duct. The mean velocity can be seen gradually increasing towards the center of the duct.

The turbulent stresses profile shows τ_{22} demonstrates a local peak much higher than τ_{12} and τ_{23}. τ_{22} normal stress component is the fluid domain's most dominant turbulent stress component.

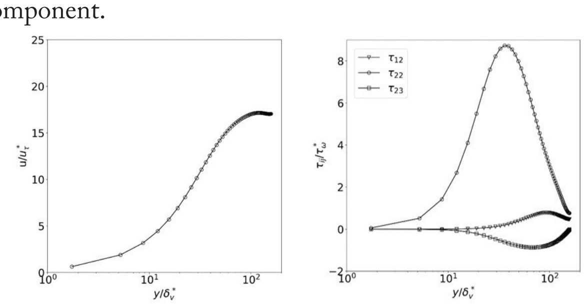

Figure 11: The profiles show the mean velocity as well as the turbulent stress components as a function of y in the square duct.

Numerical results shown in Figure 10 present anisotropic Reynolds stress tensor distributions in the quadrant of the fluid domain represented in Figure 3. Figure 10 shows the comparisons of the DNS simulated $\hat{a}^+_{12}$, $\hat{a}^+_{22}$, $\hat{a}^+_{23}$ distribution and different closure modeling approaches.

As shown in Figure 10(a), the shear stress component $\hat{a}^+_{12}$ has greater compressive strength, as indicated in blue, near the lower center of the duct. $\hat{a}^+_{22}$ normal stress components show local compressive strength, as indicated in blue near the side walls. Shear stress component, $\hat{a}^+_{23}$, appears to be uniformly distributed but the strength is the weakest.

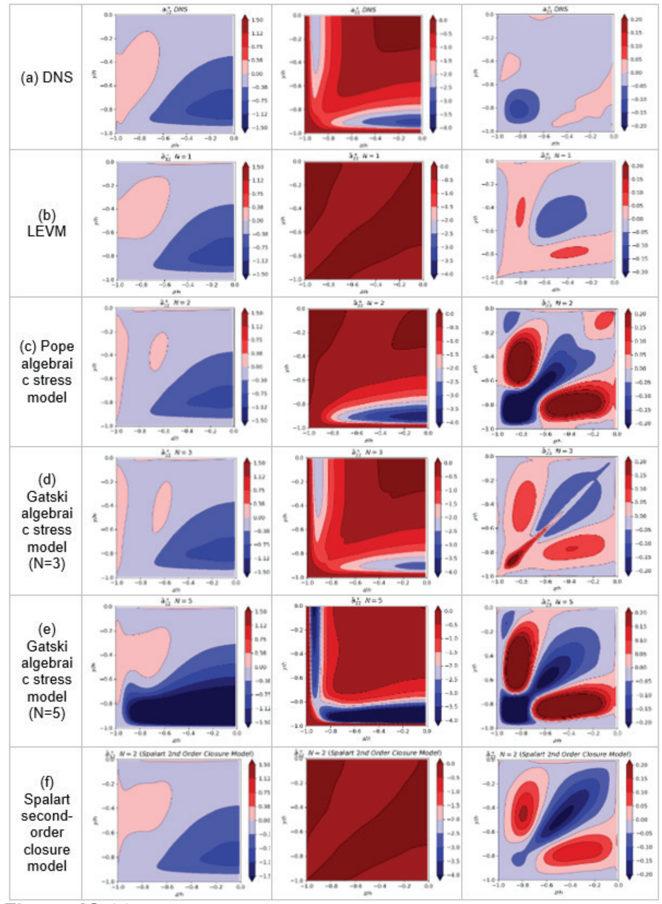

Figure 12: The comparisons of DNS computed results for the anisotropic Reynolds stress tensor $\hat{a}^+_{12}$, $\hat{a}^+_{22}$, $\hat{a}^+_{23}$ to different closure modeling approaches for square duct channel flow at Re_τ=150. (a) The DNS results show the shear stress component $\hat{a}^+_{12}$ has greater compressive strength, as indicated in blue, near the lower center of the duct. $\hat{a}^+_{22}$ normal stress components show local compressive strength, as indicated in blue near the side walls. Shear stress component, $\hat{a}^+_{23}$, appears to be uniformly distributed but the strength is the weakest. (b) The LEVM Boussinesq modelled results show $\hat{a}^+_{12}$ is in good agreement with DNS, but $\hat{a}^+_{22}$ and $\hat{a}^+_{23}$ have large discrepancies. (c) The Pope's formulation at N=2 shows $\hat{a}^+_{22}$ has improved significantly in capturing the negative compressive normal stress near the lower wall region while maintaining similar accuracy for $\hat{a}^+_{12}$ and $\hat{a}^+_{23}$ compared to LEVM. (d)(e) The Gatski's algebraic stress model shows N=5 predictions have no further improvement from N= 3, demonstrating that using more terms from Equation 11 can sometimes lead to less accuracy. (f) The Spalart's second-order closure model shows $\hat{a}^+_{12}$ is in good agreement with DNS, but $\hat{a}^+_{22}$ and $\hat{a}^+_{23}$ are found to have massive discrepancies.

Figure 10(b) shows modeled anisotropic stress tensor components using the LEVM Boussinesq model for $\hat{a}^+_{12}$, $\hat{a}^+_{22}$, and $\hat{a}^+_{23}$. The modeled $\hat{a}^+_{12}$ is closely correlated with DNS results, whereas both $\hat{a}^+_{22}$ and $\hat{a}^+_{23}$ have large discrepancies. LEVM fails to consider complex flows because it utilizes a simple linear relationship. Specifically, $\hat{a}^+_{22}$ modeled by LEVM shows more uniformly distributed than DNS, and it fails to predict the local compressive stress near the lower wall region. $\hat{a}^+_{23}$ distribution has large discrepancies with DNS results even though the magnitude is predicted within a reasonable margin.

DOI: 10.36838/v7i2.1

NLEVM - Pope algebraic stress model:

When applying Pope's algebraic stress model, the scalar function of invariants must be computed. Figure 11 shows the coefficients at different cap N values. All plots show smooth values of the coefficients, indicating minimal unphysical spatial variations for the coefficients. This allows for the coefficients to be used to compute Reynolds stress tensors.

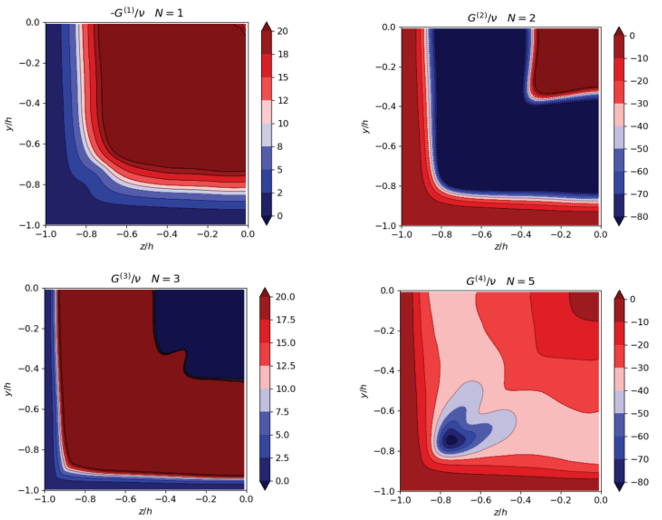

Figure 13: The contours show non-dimensional scalar coefficients $G1$, $G2$, $G3$, $G4$ for each corresponding term in Pope's nonlinear expansion. We highlight the coefficient's strength at different locations in the flow field. The area represented is the third quadrant in the flow field of the square duct.

Using Pope's formulation, Figure 10(c) shows the modeled anisotropic Reynolds stress tensor components. Overall, for N=2, the results show improved accuracy compared to linear Boussinesq approximation. In particular, $\hat{a}_{22}^{+}$ has improved significantly in capturing the negative compressive normal stress near the lower wall region while maintaining similar accuracy for $\hat{a}_{12}^{+}$ and $\hat{a}_{23}^{+}$.

NLEVM - Gatski algebraic stress model:

For N=3 and N=5, Gatski's algebraic stress model is used for more efficient computation. When using the Gatski algebraic stress model, the model's empirical coefficients are required to compute the Reynolds stress tensor. Therefore, different sets of empirical coefficients are used to compare their accuracies. The current research findings show that the Launder, Reece, and Rodi model produces the least accurate results. On the other hand, Speziale, Sarkar, and Gatski's model require additional terms, which are the most difficult to implement but give the most accurate results. Therefore, the analysis presented below is based on Speziale, Sarkar, and Gatski model.

Figure 10(e) shows both modeled Reynolds stress components at N=3 and N=5. For N=3 results show no improvement for $\hat{a}_{12}^{+}$ compared to DNS but shows improved agreement for $\hat{a}_{22}^{+}$, capturing the normal stress changes that occur in the near-wall regions. $\hat{a}_{22}^{+}$ is found to be the best accurately predicted at N=3. N=5 predictions show no improvement from N= 3, demonstrating that using more terms from Equation 11 can sometimes lead to less accuracy.

NLEVM – Spalart second-order closure model:

Figure 10(f) shows the modeled stress components using the Spalart second-order closure model. Overall, the modeling results show similar inaccuracies predictions to LEVM as shown in Figure 9(b). Compared to DNS, $\hat{a}_{12}^{+}$ shows good agreement but $\hat{a}_{22}^{+}$ and $\hat{a}_{23}^{+}$ are found to have massive discrepancies.

Figure 12 shows the qualitative correlation analysis between modeled anisotropic stress tensor components and their DNS counterparts. The direct comparison to DNS provides further insight into the quality and performance of the modeling accuracies. Compared to DNS, the linear Boussinesq-based model (N=1) shows strong correlations for $\hat{a}_{12}^{+}$ but weak correlations for $\hat{a}_{22}^{+}$ and $\hat{a}_{23}^{+}$. Overall, the analysis shows that as N increases, $\hat{a}_{22}^{+}$ shows gradual improvement until N=3. Further expansion of the terms, for example at N=5, $\hat{a}_{22}^{+}$ is found to be less accurate compared to DNS. The research findings also show $\hat{a}_{23}^{+}$ does not show any improvement with increasing N terms. This can be deemed the fact that $\hat{a}_{23}^{+}$ being the weakest in magnitude in this test case and therefore, inherently difficult to achieve the same level of accuracies as other components.

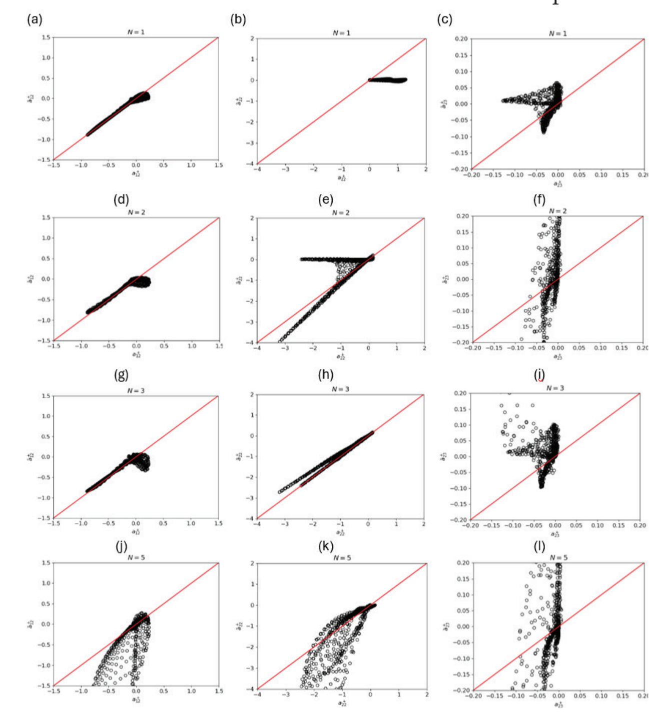

Figure 14: The qualitative analysis shows the correlation of the computed anisotropic Reynolds stress tensors, $\hat{a}_{12}^{+}$, $\hat{a}_{22}^{+}$, $\hat{a}_{23}^{+}$ and DNS data set for 3D square duct channel flow at Re_{τ}=150. Various numbers of tensor bases are simulated: (a-c) N=1; (d-f) N=2; (g-i) N=3; (j-l) N=5.

Conclusion

Turbulence is a natural phenomenon that scientists continue to study today due to its effect on the sciences. A crucial component in understanding turbulence comes from predicting turbulent behavior. The RANS model is a widespread method for predicting turbulence, allowing for cost-effective predictions. However, the RANS model introduced an additional term known as the Reynolds stress tensor that needs to be addressed with a closure model. Most turbulence models used in the field today utilize LEVM, which suffers from inaccuracy. Failure to capture the non-linear anisotropic behavior of the stress tensors must be addressed with a better non-linear modeling approach. However, research into this field is limited, and non-linear LEVM development is inconsistent and difficult to implement. The original idea of NLEVM is to exploit higher-order polynomial expansions to accurately predict complex flow with anisotropies that would otherwise not have been captured by a linear model. With turbulence modeling being such a crucial aspect of the sciences, generating accurate predictions is paramount.

This research evaluated the effectiveness of NLEVM through a computational analysis of NLEVM and LEVM performance, comparing results to high-fidelity DNS data. A 2D converging-diverging channel is tested, and the numerical results of using a linear Boussinesq model showed deficiencies. The modeled normal stress components, $\hat{a}_{11}^{+}$ showed much lower values throughout the whole channel, which does not agree with the DNS results. Shear stress component, $\hat{a}_{12}^{+}$ also showed a discrepancy, especially in the converging section of the channel. The Pope's algebraic stress model, the Gatski algebraic stress model, and the SSG model consistently showed improved predictions for $\hat{a}_{11}^{+}$ compared to the linear Boussinesq model. However, $\hat{a}_{12}^{+}$ showed similar inconsistencies in the converging area to those in the linear model.

Most real-world applications are three-dimensional; therefore, a 3D square duct case was used to evaluate LEVM and NLEVM performances. In predicting turbulence in a 3D square duct, LEVM showed good agreement with DNS for $\hat{a}_{12}^{+}$, but massive discrepancies for $\hat{a}_{22}^{+}$ and $\hat{a}_{23}^{+}$. By using the non-linear Pope algebraic stress model for *N*=2, normal stress component $\hat{a}_{22}^{+}$ has improved significantly in capturing the negative compressive normal stress near the lower wall region while maintaining similar accuracy for $\hat{a}_{12}^{+}$ and $\hat{a}_{23}^{+}$ compared to LEVM. The results of using the Gatski algebraic stress model for *N*=3, and *N*=5 showed a slightly worse turnout for $\hat{a}_{12}^{+}$, however, $\hat{a}_{22}^{+}$ predictions at *N*=3 improved drastically, correctly displaying the increased normal stress in the near-wall regions. Both LEVM and NLEVM failed to predict the shear stress component $\hat{a}_{23}^{+}$. The Spalart second-order closure model predictions yielded similar results to LEVM, with relatively accurate a_{12}^{+} predictions but major downsides for $\hat{a}_{22}^{+}$ and $\hat{a}_{23}^{+}$. Overall, it was shown that NLEVM experiences higher accuracy for $\hat{a}_{22}^{+}$, but $\hat{a}_{23}^{+}$ is unable to be predicted by any model. This can be attributed to the fact that $\hat{a}_{23}^{+}$ is the weakest in magnitude in this test case; therefore, achieving the same level of accuracy is inherently difficult as other components. The lack of improvement from *N*=3 to *N*=5 also demonstrates that using higher-order terms can sometimes be unnecessary.

Through current analysis, this research demonstrates there is still significant room for improvement in the NELVM predictions of the Reynolds stress tensor. Future research on the ability of machine learning or optimization techniques to improve predictions can be promising and have potentially groundbreaking implications.

Acknowledgments

I would like to thank my parents for their continued support of my research and encouragement throughout the process. They continuously helped me and offered words of advice during periods of struggle. I would also like to show appreciation to my science research teacher at school and my mentor, Fong Pan, for the invaluable help and support they consistently gave me throughout this project.

References

1. Schmitt, F., About Boussinesq's turbulent viscosity hypothesis: historical remarks and a direct evaluation of its validity. *Comptes Rendus Mecanique*. **2007**, *335* (9-10), 617-627. DOI: 10.1016/j.crme.2007.08.004
2. Lumsey, J., Toward a turbulence constitutive equation. *Journal of Fluid Mechanics*. **1970**, *41* (2), 413-434. DOI: 10.1017/S0022112070000678
3. Pope S. B., A more general effective-viscosity hypothesis. *Journal of Fluid Mechanics*. **1975**, *72* (2), 331-340. DOI: 10.1017/S0022112075003382
4. Gatski T. B., On explicit algebraic stress models for complex turbulent flows, *Journal of Fluid Mechanics*. **1993**, *254*, 59-78. DOI: 10.1017/S0022112093002034
5. Spalart P. R., Strategies for turbulence modelling and simulations, *International Journal of Heat and Fluid Flow*, **2000**, *21* (3), 252-263. DOI: 10.1016/S0142-727X(00)00007-2
6. Modesti D., A priori tests of eddy viscosity models in square duct flow, *Theoretical Computational Fluid Dynamics*, **2020**, *34*, 713-734. DOI: 10.1007/s00162-020-00545-9
7. *NASA's Turbulence Modeling Resource*. https://turbmodels.larc.nasa.gov/index.html
8. Direct numerical simulation dataset of turbulent square duct flow. 4TU Research Data. n.d. https://data.4tu.nl/articles/_/12763709/1
9. Hunter, J.D., Matplotlib: A 2D Graphics Environment, *Computing in Science & Engineering*, **2007**, *9* (3), 90-95. DOI: 10.1109/MCSE.2007.55

Author

Aiden Kwon is a dedicated science researcher who has worked extensively in his fields of interest. In Aiden's sophomore year, he had the honor of attending the International Science and Engineering Fair. Aiden appreciates his experience at ISEF as being one of the most memorable times of his life.

DOI: 10.36838/v7i2.1